© 2023. Published by The Company of Biologists Ltd | Journal of Experimental Biology (2023) 226, jeb244857. doi:10.1242/jeb.244857

RESEARCH ARTICLE

Foot extension and retraction in the clam *Calyptogena okutanii* without any Keber's valve: an inflatable fastener bag model

Eriko Seo[1], Kazue Ohishi[2,*], Yoshie Imaizumi-Ohashi[3], Mika Yokoi-Hayakawa[3], Tsuyoshi Yamaguchi[4] and Yoshiteru Seo[5,‡]

ABSTRACT

In order to investigate the foot manipulation of a clam without a Keber's valve, *Calyptogena okutanii* was examined by light microscopy, magnetic resonance imaging and computed tomography. The foot chamber was divided into two compartments by a dense muscle fastener zone (FZ) comprising a pedal artery and sinuses in the mid-sagittal plane in between muscles running in the anterior–posterior oblique direction. The distal part of the foot chamber (inflatable fastener bag, IFB) had a loose superficial muscle layer. The proximal part of the foot chamber (visceral reservoir, VR) was covered by a dense superficial muscle layer. The outlet of the VR was connected with the hinge ligament duct, consisting of the hinge ligament, a pair of shells and the pericardium. Based on these anatomical structures, foot extension starts from contraction of muscles in the FZ, so that flow in the FZ is stopped. Then, the superficial muscles of the foot contract, and the pressure of the IFB increases so that the foot can extend. Foot retraction starts from the relaxation of muscles in the FZ so that the hemolymph returns to the VR. The hinge ligament duct allows a constant return flow from the foot chamber to the gills and the heart. The heart rate and the flow in the FZ, which decreased and increased during the foot extension and retraction, respectively, supported this model. In conclusion, the FZ of *Calyptogena okutanii* could be an alternative to Keber's valve in *Anodonta*, playing a similar role.

KEY WORDS: Bivalvia, *Phreagena*, Burrowing, Foot chamber, Keber's valve, Heart rate, MRI

INTRODUCTION

The foot extension and retraction processes in the burrowing of clams have been studied for many years (Morton, 1964; Brand, 1972; Trueman, 1983; Trueman et al., 1986; Winter et al., 2012). Despite using the digging cycle, digging into the sand requires a much higher force exerted by the foot compared with moving on the surface of the sand. In *Anodonta*, the peak pressure caused by foot extension (15–30 cm H_2O) is much higher than the ventricular pressure (5 cm H_2O) (Brand, 1972). This force is caused by the high pressure in the pedal sinus that is believed to be produced by contraction of the ventricular muscle and pedal circular muscles (Trueman, 1983; Ruppert at al., 2015). This model has one outstanding issue. Because the bivalves have an open circulation system, the high pressure in the foot must apply to the epithelium of the visceral organs, gills and mantles. It seems that there is some danger of damage to such delicate structures (Truman et al., 1966). For example, most of the surface of the visceral mass is covered with a simple columnar epithelium without any superficial muscle layer. This epithelium alone cannot tolerate the high pressure required for foot extension. In a previous report on a fresh water clam, *Nodularia douglasiae*, we identified the structure of the foot chamber (Seo and Seo, 2019) as a closed space that consists of the superficial muscle layers of the foot, the anterior aorta (an inlet) and Keber's valve (an outlet). Keber's valve is a sphincter muscle that separates the proximal end of the pedal sinus and the visceral sinus that goes to the kidneys and gills (Brand, 1972; Keber, 1851; Seo and Seo, 2019). Extension of the foot starts with the relaxation of the pedal circular muscle, then Keber's valve closes and prevents the return flow of the hemolymph, so that the hemolymph fills in the pedal hemocoel and the foot volume increases (Bayne, 1976; Trueman and Brown, 1985; McMahon et al., 2011). Then, the pedal circular muscle in the superficial muscle layer contracts and the pressure in the pedal hemocoel is increased. As a result, the foot extends. Retraction of the foot is initiated by the opening of Keber's valve to release hemolymph from the pedal hemocoel. Therefore, Keber's valve, or a similar structure, is thought to be an essential structure for the burrowing process (Trueman et al., 1966). However, reports on the presence of Keber's valve are limited to *Anodonta*, *Donax* and *Nodularia* (Keber, 1851; Willem and Minne, 1898; Schwanecke, 1913; Brand, 1972; Trueman and Brown, 1985; Seo and Seo, 2019). The presence of Keber's valve, or a similar structure, has not been described in clams, such as *Mercenaria* and *Mya* (Ansell and Trueman, 1967; Trueman, 1966). After light microscopy examination of more than 2000 hematoxylin and eosin (HE) stained slices, we could not detect Keber's valve in a deep-sea clam, *Calyptogena okutanii* (E.S., Y.I.-O., M.Y.-H. and Y.S., unpublished observation). *Calyptogena* clams are one of the dominant benthic bivalves in the chemosynthetic community in the Off Hatsushima Island region (Kojima, 2002; Kojima and Ohta, 1997; Hashimoto and Okutani, 1994). *Calyptogena* clams are active bivalves in the deep-sea, and take H_2S via feet extending into the mud to obtain a supply of endosymbiotic chemosynthetic bacteria (Hashimoto and Okutani, 1994; Childress et al., 1993). *Calyptogena okutanii* is one of the most difficult species to maintain in normal atmospheric conditions, so experiments must be conducted within 2–3 days of sampling (Miyake et al., 2012; Seo et al., 2022). In regard to the present study, we obtained 5 clams within 24 h of sampling. This is the minimum sample size for which it is possible to get results with statistical significance. We applied a

[1]Central Laboratory, Marine Ecology Research Institute, Onjuku, Chiba 299-5105, Japan. [2]Japan Agency for Marine-Earth Science and Technology, Yokosuka, Kanagawa 237-0061, Japan. [3]Research Center for Advanced Medical Science, Dokkyo Medical University School of Medicine, Mibu, Tochigi 321-0293, Japan. [4]Department of Anatomy, Dokkyo Medical University School of Medicine, Mibu, Tochigi 321-0293, Japan. [5]Division of Cell Structure, National Institute for Physiological Sciences, Okazaki, Aichi 444-8787, Japan.
*Present address: Faculty of Health and Medical Sciences, Kanagawa Institute of Technology, Atsugi, Kanagawa 243-0292, Japan.

‡Author for correspondence (yseo@nips.ac.jp)

E.S., 0000-0003-0879-9083; Y.S., 0000-0001-9775-4738

Received 5 August 2022; Accepted 5 December 2022

precise and non-invasive technique, magnetic resonance imaging (MRI), which made it possible to obtain anatomical and functional data from the samples. In addition, we obtained micro-computed tomography (micro-CT) images and HE-stained slices, so that the small sample number issue was minimized.

In this study, we investigated the mechanism of foot extension and retraction in the absence of Keber's valve. First, we investigated the muscular and vascular structure of the foot using HE-stained slices and T_1-weighted gradient-echo magnetic resonance imaging (T_{1w}-MRI), and tried to identify an alternative mechanism for controlling the flow of hemolymph in the foot. Second, we investigated the anatomical structure of the hinge, including the heart and gills using micro-CT, T_{1w}-MRI and HE-stained slices, and tried to find an alternative route for the hemolymph to return to the heart. Third, we built a model for foot extension and retraction without Keber's valve, based on the anatomical results. Finally, we estimated: (1) the changes in the volume and flow of hemolymph in the foot and (2) the changes in pressure in the vessels and the foot from T_{1w}-MRI of living clams during the resting, foot extension and retraction time periods. Pressure was indirectly estimated from the heart rate using Frank–Starling's law of the heart. The model was tested by comparison with these physiological results.

MATERIALS AND METHODS

Experimental animals

Five *Calyptogena okutanii* (Kojima and Ohta, 1997) were collected using the remotely operated vehicle (ROV) *Hyper-Dolphin*, operated by the research vessel *Natsushima* of the Japan Agency of Marine-Earth Science and Technology. Three clams were collected at the Off Hatsushima Island seep sites in Sagami Bay at a depth of 858 m (35°00.966 N, 139°13.329 E, Dive HPD#1644) during cruise NT14-05 (6 April 2014), and two more clams were collected at a depth of 857 m in Sagami Bay (35°00.954 N, 139°13.327 E, Dive KM-ROV#18) during the KM16-04 cruise (4 July 2016), operated by the research vessel *Kaimei* of the JAMSTEC. The clam species was identified by sequencing the mitochondrial cytochrome oxidase subunit I gene using DNA extracted from the foot with a DNeasy Blood and Tissue Kit (Qiagen, Hilden, Germany) as a template (Watanabe et al., 2013). The length, height and width of the *C. okutanii* individuals were 36.9±3.0 mm, 20.8±1.3 mm and 11.9±0.9 mm (mean±s.d., n=5), respectively.

The collected clams were kept in natural seawater in aquarium tanks at 4°C during the cruises. At the laboratory, each clam was kept in non-aerated synthetic seawater (salinity 36‰) in 0.5 l baths at 5°C. Under these conditions, the clam can survive for 6 days (Seo et al., 2022). All of the animal experiments conducted in this study were carried out under the rules and regulations of the 'Guiding Principles for the Care and Use of Animals' set by the Physiological Society of Japan, and approved by the Animal Research Councils at Dokkyo University School of Medicine (#840).

MRI

^{1}H magnetic resonance (MR) images were obtained with ParaVison operating software (version 5.1), using a 7 T microimaging system (AVANCE III, Bruker Biospin, Ettlingen, Germany) equipped with an active shielded gradient (micro2.5) and a 25 mm ^{1}H linear radiofrequency coil. The clams were immersed in synthetic seawater without aeration, and the temperature was kept at 10°C (Seo et al., 2014a; 2022).

The motion of the heart and the flow of the hemolymph were imaged by the inflow effect of T_1-weighted gradient-echo imaging (T_{1w}-MRI) (Bock et al., 2001; Seo et al., 2014b). The typical sagittal imaging parameters used for the *in vivo* T_{1w}-MRI were as follows: 48×24 mm field of view (FOV) with a 192×96 data matrix and a slice thickness of 2 mm, 20 ms relaxation delay (T_R), 3.5 ms echo-time (T_E), 45 deg flip angle (FA) and 1 accumulation. A transverse image was obtained by 24×24 mm FOV with a slice thickness of 1 mm. Each MRI measurement session consisted of 128 or 256 images obtained every 1.92 s. For higher heart rates, images were obtained every 0.64 s using 64×64 data matrix or every 1.28 s using 128×128 data matrix with a combination of T_R/T_E/FA=10 ms/3.5 ms/32.5 deg. In order to adjust the inflow effect of T_{1w}-MRI for a shorter TE, the flip angle was decreased (Fig. S1) (Seo et al., 2014b). The increase in the image intensity of T_{1w}-MRI is roughly proportional to the flow velocity of the hemolymph. The heartbeat was detected by an increase in the T_{1w}-MRI intensity of a region of interest (ROI) located on the auriculoventricular (AV) valve. The heart rate was calculated from the beat–beat interval, and is presented as beats min^{-1}.

We did not expect to accurately show the position and shape of the foot, especially outside the shells, but the position of the foot is relatively restricted inside the shells. Therefore, we carried out two semi-quantitative analyses of the 2D T_{1w}-MR images: (1) estimation of the changes in the hemolymph flow in a specific part of the foot, based on the increase in T_{1w}-MR image intensity in a given ROI on the foot, and (2) detection of any extension or retraction of the foot, based on the area of the foot in a given ROI set inside the shells. The ROI was set on the foot so that it would cover movement of the foot from the resting stage to full extension of the foot. Foot pixels that showed an intensity level more than a given threshold were selected. The threshold we applied was typically 30% of the maximum image intensity. Relative changes in the area of the foot were estimated from the total number of pixels. Note, the value of any relative changes in the area is only valid to detect any qualitative extension or retraction the foot.

Anatomical information was obtained by 3D MRI. The imaging parameters used for *in vivo* 3D T_1-weighted gradient-echo imaging (3D T_{1w}-MRI) were 46.08×23.04×23.04 mm FOV with a voxel size of 180×180×180 µm, a combination of T_R/T_E/FA=50 ms/3 ms/45 deg and a total image acquisition time of 27 min 18 s. When it was necessary to enhance the vascularity image, the clams were incubated in 1 mmol l^{-1} gadolinium-diethylenetriamine pentaacetic acid (GdDTPA) for 1.5 days. After the *in vivo* MRI experiments, 3 clams were fixed with synthetic seawater containing 4% paraformaldehyde (PFA) for 1 week at 5°C. For the PFA-fixed species, high-resolution 3D T_{1w}-MRI was measured with a voxel size of 90×90×90 µm with a combination of T_R/T_E/FA=50 ms/3.5 ms/45 deg and a total image acquisition time of 7 h 16 min.

Micro-CT

Anatomical information of the PFA-fixed clams was obtained by an X-ray micro-CT imager (Rigaku R-mCT2, Rigaku, Japan). The samples were imaged with a source voltage of 90 kV and a source current of 160 µA. 3D CT images had a 24×24×19 mm FOV with a voxel size of 47×47×47 µm and a total image acquisition time of 4 min 30 s.

Histology

For the histological studies, the paraffin sections of the PFA-fixed clams were prepared using a slice thickness of 10 µm. The sections were stained with HE. Images were detected by microscopy (BZ-X710, Keyence, Osaka, Japan; BX63, Olympus, Tokyo, Japan)

with image-stitching mode. Low-magnitude images were detected using a stereomicroscope (SZX16, Olympus, Tokyo, Japan).

Statistics

Observed values are presented as means±s.d. with the number of samples (n). Significant differences of means were tested using the one-sample two-sided t-test, and significant differences of means between two means were tested using the two-sample two-sided t-test employing Excel 2016 (Microsoft, Redmond, WA, USA). A statistical difference was detected by one-way ANOVA for 3 groups, and also detected for all combinations by Tukey multiple comparisons of means employing Easy R Statistics software (EZR v2.7-1) with R (http://www.R-project.org/, v.3.6.3) (Kanda, 2013). P-values less than 0.05 were regarded as significant. Sample size was estimated by EZR v2.7-1. In cases where the sample size is 5, the minimum difference is 1.8 s.d. in order to discriminate between the two groups with a two-sided α error of 0.05 and a power of 0.8.

RESULTS

Structure of the foot of *Calyptogena okutanii*

The anatomical structure of the foot was examined in the HE-stained image and by T_{1w}-MRI of the PFA-fixed clam compared with the histological anatomy of bivalves (Prudie, 1887; Borradaile and Potts, 1935; Klylova and Sahling, 2006; Seo et al., 2022). As shown in transverse sections at the position of the visceral ganglion (Fig. 1A,E), the transverse section of the foot is an inverse spade shape. The surface of the foot is covered with a simple columnar epithelium, with a muscle layer running underneath (Fig. 1A,L–N). The pedal sinuses are lined up in the mid-sagittal plane (Fig. 1A,E–G). In the distal part (heart-shaped part) of the foot (Fig. 1B), the superficial muscle layer consists of low-density muscle fibers, including circular muscles (Fig. 1L,O). In the inner parts of the foot, the density of the muscle fibers decreased, and the orientation of the fibers varied, such as in the dorsal–ventral, anterior–posterior and right–left directions, and formed the pedal hemocoel (Fig. 1B,L,O). This part enlarged during foot extension. So, we named the distal part of the foot chamber the ‘inflatable fastener bag’. The proximal side of the foot (handle part of the spade: Fig. 1D) is covered by high-density superficial muscle layers running in the dorsoventral direction and muscles running around the foot chamber (circular muscles; Fig. 1N), and extending to the dorsal side of the shell (Fig. 1D). In the inner parts of the foot chamber, there are gastrointestinal ducts, digestive glands and gonad cells. We named this part the ‘visceral reservoir’. In the distal part of the handle of the spade (neck part), arteries and sinuses were narrowed by the dense muscles (Fig. 1I). As shown in a sagittal section, most of the muscle fibers run in the anterior–posterior oblique direction (Fig. 1G,P), but some run in the right–left direction (Fig. 1M). We named this space the ‘fastener zone’ (Fig. 1C). In sections at the visceral ganglion (Fig. 1J) and on the more dorsal side (Fig. 1K), the visceral sinuses are dilated, divided and disappear into the tissue (Fig. 1F,G).

The structure around the hinge of *C. okutanii*

In order to examine the venous return pathway to the heart, the anatomical structure around the hinge was examined by micro-CT and T_{1w}-MRI, and the HE-stained image of the PFA-fixed clam was compared with the histological anatomy (Ruppert et al., 2015; Klylova and Sahling, 2006). The hinge was visualized by 3D constructed micro-CT (Fig. 2A,B). The Ω-shaped hinge ligament was depicted at high and low intensity by micro-CT and T_{1w}-MRI, respectively (Fig. 2B,D–G). It consisted of dense fibrous tissue (Fig. 2H–J). The ligament covered the area from the teeth to the posterior part of the shell, for a distance of 7.5±1.6 mm (n=3), which is around 20% of the length of the shell (Fig. 2B,D–G,H–K). The hinge ligament, a pair of shells and the pericardium form a duct structure with the largest transverse diameter of 1.58±0.07 mm (n=3) (Fig. 2B,F). We named this duct the ‘hinge ligament duct’. The hinge ligament duct was filled with hemolymph (Fig. 2Hii,iii, Kiii), and connected between the outlet of the muscle chamber and the gills and the heart (Fig. 2C,Iii,Jii,Kii). In the hinge teeth, the outer mantle epithelium continued and covered the inner surface of the hinge and the hinge ligament duct (Fig. 2Hii). As far as we could tell by examining the HE-stained images, the teeth were not in direct contact with each other. The posterior end of the inlet of the hemolymph, from the foot chamber to the hinge ligament duct, is indicated by an asterisk in Fig. 2Iii. Around the posterior end of the hinge ligament duct, there were efflux pathways which were open to the gills and the heart (Fig. 2Jii,Kii). Keber’s valve, if present, is expected to be located near the abdominal side of the heart with a large visceral sinus (Keber, 1851). However, in this study, we did not detect Keber’s valve, either in HE-stained slices or in the high-resolution MRI.

Vasculature of the foot of living *C. okutanii*

The vasculature from the heart to the foot was examined by T_{1w}-MRI of a living clam. After incubation in 1 mmol l^{-1} GdDTPA seawater for 1.5 days, vessels appear white compared with the adjacent tissues (Fig. 3). The arterial system was depicted from the ventricle of the heart to the aorta. One arterial branch ran down to the foot, passing through the fastener zone. It seemed to be a single artery entering the distal part of the foot. Pedal sinuses extended from the distal part of the foot, lined up in the mid-sagittal line, and passed through the fastener zone to the visceral side. The visceral sinuses were not unified into a single sinus, but were instead divided into the visceral tissues. We could not find any valve structure like Keber’s valve, or a large visceral sinus.

Heartbeat of *C. okutanii* during foot extension and retraction

From the 58 MRI sessions obtained from 5 clams at 2–3 days after sampling, we obtained 22 sessions with regular heartbeats without any significant foot motion. Typical heartbeat images in the resting state are shown in Fig. 4. Diastole of the heart was detected by any increase in the signal intensity of the AV valve, which indicates inflow from the auricle to the ventricle (Fig. 4Ai). Systole of the heart was detected by any increase in the signal intensity of the aorta or the pedal artery, which is caused by ejection of hemolymph from the ventricle (Fig. 4Aii). The heartbeat was detected by an increase in the T_{1w}-MRI intensity of an ROI on the AV valve (Fig. 4Aiii). The average heart rate of the 18 heartbeats shown in Fig. 4C was 6.0 ±0.5 beats min^{-1}. As shown in Fig. 4Ci, the peak position of the pedal artery (systole) was delayed by 3.7±0.8 s (18 heartbeats) from that of the AV valve (diastole). This delay was almost 37% of the beat–beat interval. The ROI for detection of flow was set on the area of the fastener zone of the foot (Fig. 4Aiii), and there were no significant peaks in the ROI, with almost constant values (Fig. 4Cii). The ROI for detection of extension and retraction of the foot was set on the foot, so that it would cover movement of the foot from the resting stage to the full extension of the foot (Fig. 4Bi). The histogram of the image intensity of the ROI consisted of the foot and the seawater (Fig. 4Bii). Pixels for the foot are shown in red in Fig. 4Biii, and the histogram corresponding to the foot is shown in Fig. 4Biv. A minimal movement of the foot was detected at around 80 s that caused a small decrease in the relative area of the foot

Journal of Experimental Biology (2023) 226, jeb244857. doi:10.1242/jeb.244857

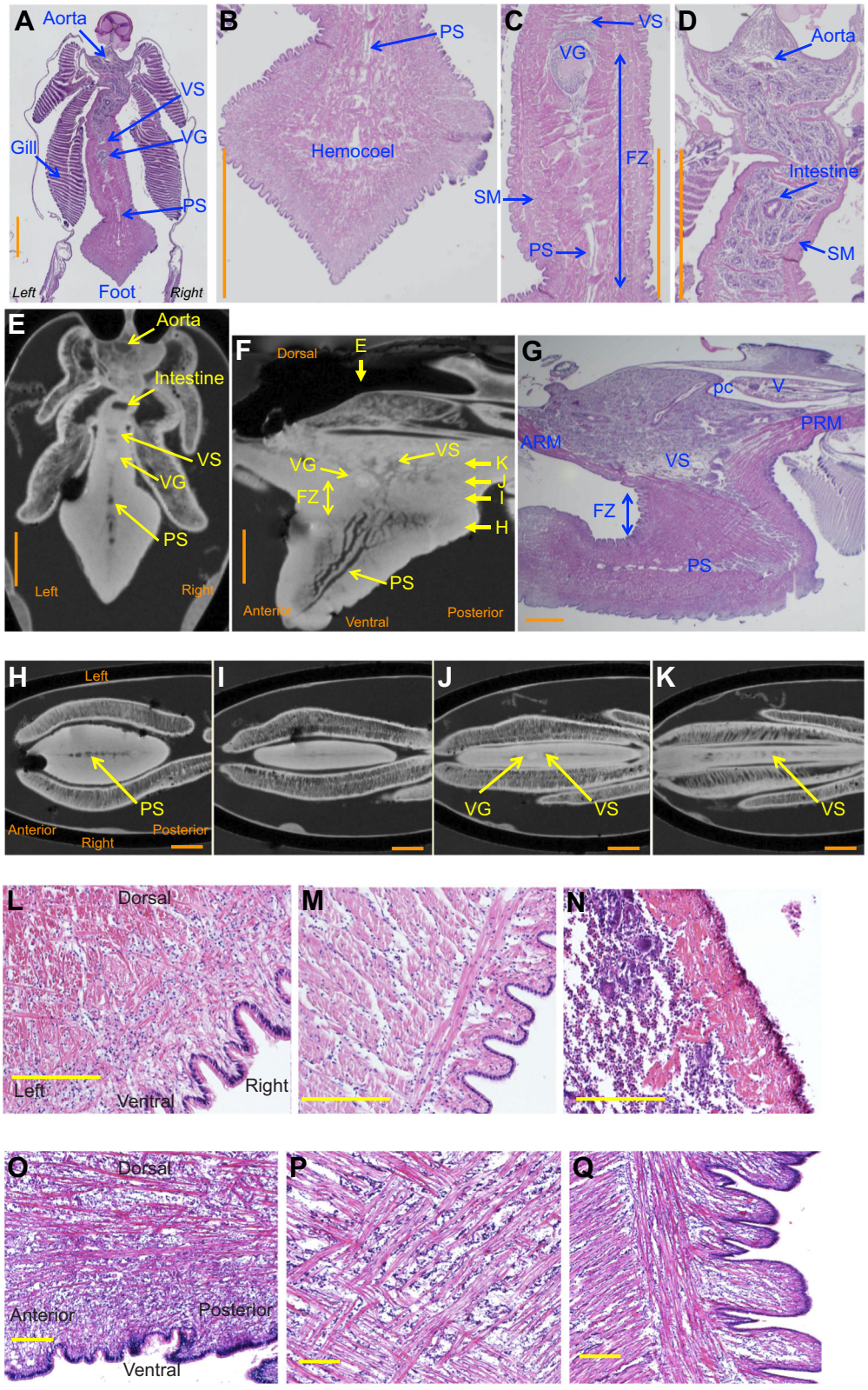

Fig. 1. Anatomical structure of the foot of *Calyptogena okutanii*.
(A–E) Transverse images of the paraformaldehyde (PFA)-fixed clam. Orange scale bars: 2 mm.
(A) Transverse hematoxylin–eosin (HE)-stained section at the visceral ganglion (VG). The foot is covered with a superficial muscle (SM) layer that forms the foot chamber. VS, visceral sinus; PS, pedal sinus. (B) Distal part of the foot, named the 'inflatable bag'. (C) Middle part of the foot, named the 'fastener zone' (FZ). (D) Proximal part of the foot, named the 'visceral reservoir'. (E) Transverse T_1-weighted magnetic resonance (T_{1w}-MR) image at the position corresponding to A.
(F,G) Sagittal images of the PFA-fixed clam. (F) Mid-sagittal T_{1w}-MR image. The PS and VS are shown in black, and are lined up in the mid-sagittal plane. The position of the section is indicated by arrows labelled E and H–K. (G) Mid-sagittal HE-stained image. ARM, anterior retractor muscle; pc, pericardial cavity; PRM, posterior retractor muscle; V, ventricle.
(H–K) Coronal T_{1w}-MR images of the foot. Orange scale bars: 2 mm.
(H) 2.5 mm ventral side from the VG. Dilated PS are lined up in the mid-sagittal line. (I) The FZ, 0.8 mm ventral side from the VG. The PS are hard to see in the dense muscle layer.
(J) Section at the level of the VG. The VG are lined up in the mid-sagittal line.
(K) 1.0 mm dorsal side from the VG. Dilated VS are distributed.
(L–N) Transverse HE-stained images. Yellow scale bars: 200 µm. (L) Muscle fibers and hemocoel in the inflatable bag. (M) The FZ. (N) Superficial muscle layer of the visceral reservoir.
(O–Q) Sagittal HE-stained images. Yellow scale bars: 200 µm.
(O) Anterior–posterior directed muscle in the inflatable bag. (P) Anterior–posterior oblique muscles in the FZ. (Q) Superficial muscle layer of the FZ.

(Fig. 4Cii). However, the heart rate before and after movement was 6.1±0.4 beats min^{-1} (8 heartbeats) and 5.8±0.6 beats min^{-1} (9 heartbeats), respectively. Thus, that minimal movement of the foot had almost no effect on heartbeat (Fig. 4C).

Typical changes in heartbeat during a series of resting, extension and retraction of the foot are shown in Fig. 5 and Movie 3. The decrease in the relative area of the foot relative to the extension of the foot started at 53 s, and the increase in the relative area of the foot relative to the retraction of the foot started at 130 s (Fig. 5Aii). In the resting state, the heart rate was regular (6.0±0.4 beats min^{-1}, 5 heartbeats). During foot extension, the heartbeat decreased and almost stopped at the end of extension.

Journal of Experimental Biology (2023) 226, jeb244857. doi:10.1242/jeb.244857

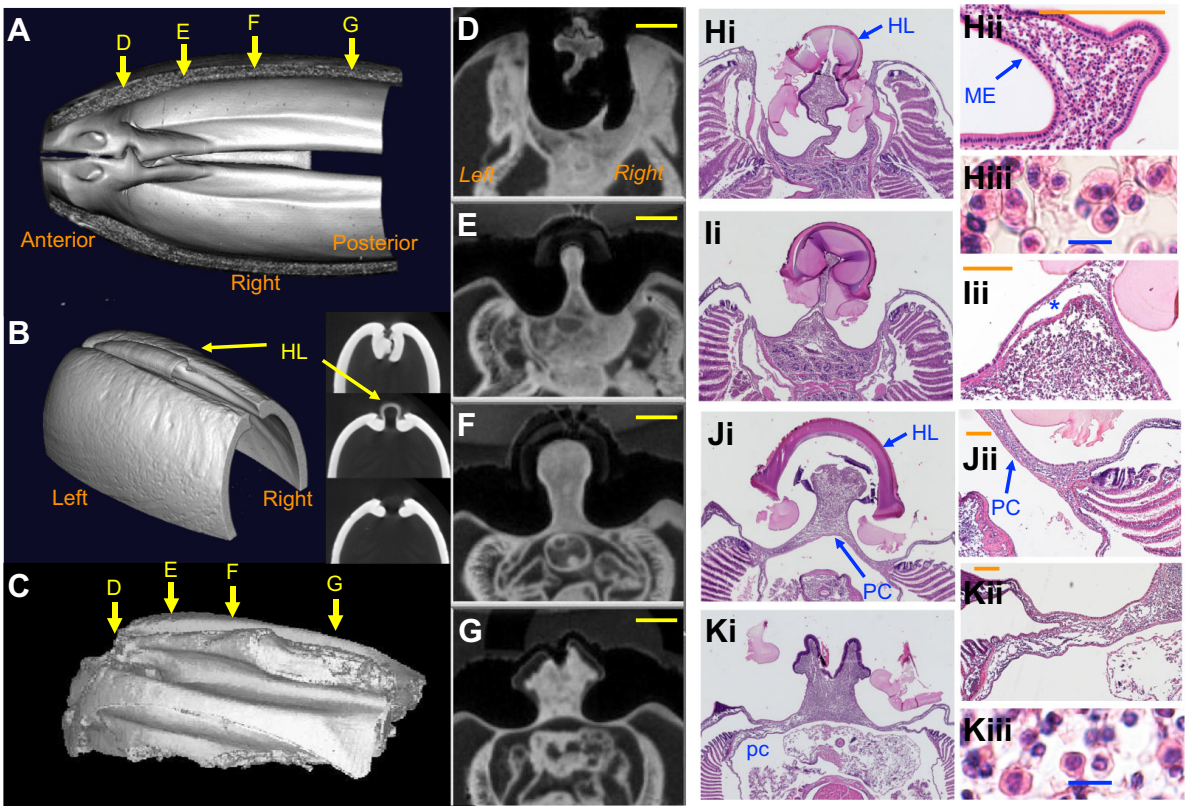

Fig. 2. Anatomical structure around the hinge of the PFA-fixed *C. okutanii*. (A–C) 3D reconstructed images. (A) Ventral view of shells by micro-computed tomography (micro-CT). The shells are depicted in white. The position of the section is indicated by arrows labelled D–G. Refer also to Movie 1. (B) Posterior–dorsal view of the shells and hinge by micro-CT. The hinge ligament (HL) and the pair of shells form a duct structure (hinge ligament duct). The transverse images correspond to slices of D, F and G from the top to the bottom. Refer also to Movie 2A. (C) Posterior–dorsal view of the hemolymph and visceral tissues around the hinge by T_{1w}-MRI. The hinge ligament duct is filled with hemolymph, and is connected to the visceral tissues. Refer also to Movie 2B. (D–G) Transverse T_{1w}-MR images. Yellow scale bars: 1 mm. (D) Transverse image at the cardinal teeth, 2.7 mm anterior from the VG. (E) Transverse image at the VG. (F) 3.7 mm posterior from the VG. (G) 8.4 mm posterior from the VG. (H–K) HE-stained images corresponding to images D–G. Orange and blue scale bars: 200 µm and 10 µm, respectively. (Hii) Higher magnitude image of the hinge. The outer mantle epithelium (ME) continues and covers the inner side of the hinge and the hinge ligament duct. (Hiii) Hemolymph cells in the hinge ligament duct. (Iii) Posterior end of the inlet of the hemolymph from the foot chamber to the hinge ligament duct (*). There is no valve structure. (Jii, Kii) Pathways from the hinge ligament duct to the gill. The ventral side of the hinge ligament duct is covered by the pericardium (PC). (Kiii) Hemolymph cells in the distal part of the hinge ligament duct. The number of interstitial fibrous cells was higher than that in the initial part of the duct (Hiii).

When retraction started, the heartbeat recovered quickly, at a heart rate of 7.1±0.6 beats min^{-1} (5 heartbeats). The increase in the image intensity of the fastener zone (‡, § and ¶ in Fig. 5Aii) indicated an increase of flow in the foot, and the slow decrease in the image intensity during extension indicated a decrease in the flow in the fastener zone. These changes in the flow were estimated to be of the order of 0.5–1.0 mm s^{-1} (Fig. S1). The spikes in Fig. 5Aii at around 120 s (labeled e) are artifacts caused by a large motion of the foot (Fig. 5Be). The image intensity of the hinge ligament duct presented minimal changes during resting, extension and retraction of the foot (Fig. 5Ai). Among the 58 MRI sessions obtained from 5 clams at 2–3 days after sampling, we got obtained 5 sets of resting–extension–retraction series of the foot from 3 clams. The heart rate at rest, extension and retraction of the foot was 5.8±0.4, 3.8±1.1 and 7.3±0.4 beats min^{-1}, respectively, each showing statistically significant differences from each other (P<0.01) (Fig. 5C). Therefore, compared with that during the resting state, the heart rate decreased and then increased during extension and retraction of the foot. The relative image intensity of the hinge ligament duct is presented compared with the resting state in Fig. 5D. There were no significant changes during extension and retraction of the foot (P>0.05).

DISCUSSION

A model of foot extension and retraction without Keber's valve

The foot and related circulation system of *C. okutanii* was analyzed using high-resolution 3D T_{1w}-MR images, micro-CT and light microscope images of HE-stained specimens. A model of the foot and circulation system is summarized in a schematic diagram of the mid-sagittal section in Fig. 6. The foot is covered by a superficial muscle layer, which forms the foot chamber (Seo and Seo, 2019). The inlet to the muscle chamber is the aorta, and there is an outlet just underneath the hinge without any valve structure. The foot chamber consists of two compartments (the inflatable fastener bag and the visceral reservoir) divided by the fastener zone (Fig. 1A–D). The inflatable fastener bag is the distal part of the foot (the heart-shaped part; Fig. 1E) and it is covered by low-density superficial muscles, so that it forms a high compliance wall (Fig. 1B,L). Therefore, the distal part of the foot chamber could inflate as a result of an increase in interstitial pressure. We could not detect any valve similar to Keber's valve (Keber, 1851) in *C. okutanii*. We did find an interesting structure in the fastener zone in the neck part of the foot (Fig. 1C,G). The high-density muscle fibers ran in the anterior–posterior oblique direction and the right–left direction

Journal of Experimental Biology (2023) 226, jeb244857. doi:10.1242/jeb.244857

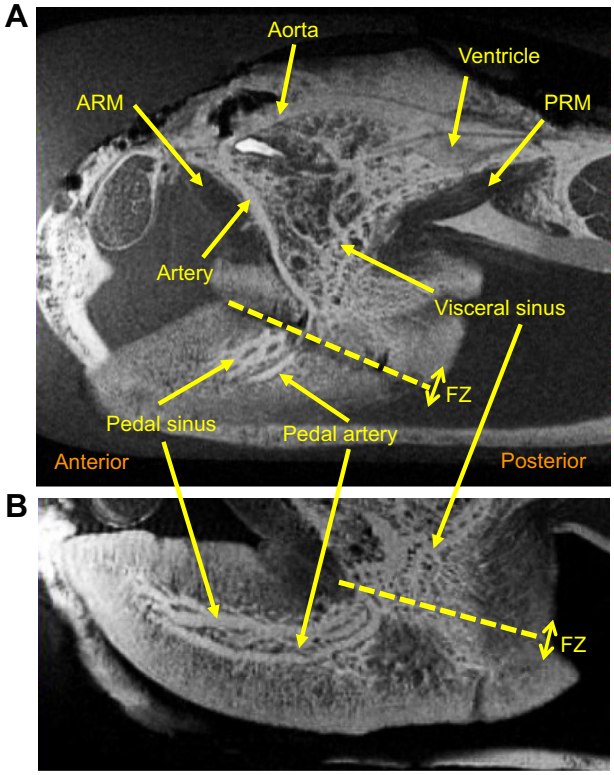

Fig. 3. Vascular structure of the foot of a living *C. okutanii* measured by T_{1w}-MRI. The clam was incubated in 1 mmol l^{-1} GdDTPA seawater for 1.5 days. (A) Mid-sagittal image of a living clam. (B) Mid-sagittal image of the foot. Vessels appear white. The dashed yellow lines indicate the direction of the FZ.

(Fig. 1G,M,P). The pedal arteries and pedal sinuses pass in the mid-sagittal line (Fig. 1F,H). Therefore, when the muscle in the fastener zone contracts strongly, the flow in the pedal arteries and pedal sinuses should be stopped, so that the pressure of the hemocoel in the inflatable bag is increased by the contraction of the pedal circular muscles. The pedal sinuses come together in the fastener zone, then they are divided into branches on the proximal side of the foot chamber (the visceral reservoir) (Fig. 1F). These sinuses are just like the portal venous system which can control the flow of the hemolymph precisely. The FZ could be an alternative to Keber's valve, playing a similar role. As in the muscle chamber system with Keber's valve, such as seen in *Nodularia* (Seo and Seo, 2019), the internal pressure in the muscle chamber has to increase equivalently with extension of the foot. In the system containing the fastener zone, the increase of pressure confined in the distal part of the foot and the changes of pressure in the proximal side of the muscle chamber must be much smaller than those caused by the single compartment system with a Keber's valve. In addition, the smaller volume of the inflatable fastener bag promises an efficient way to extend the foot by the cardiac output of the hemolymph.

We named the proximal part of the foot chamber the 'visceral reservoir', which might be a temporary reservoir of hemolymph from the inflatable fastener bag. After passing the fastener zone, the visceral sinus divides and disappears in the interstitial space of the foot chamber (Fig. 1F), and it is not likely to be combined again into a large longitudinal visceral sinus, as found the *Nodularia* (Seo and Seo, 2019). We could not find any Keber's valve at all, which is supposed to be positioned at the anterior of the longitudinal visceral sinus (Seo and Seo, 2019). The interstitial pressure might be at around 1 cm H_2O, as estimated from pressure in the pericardial cavity (Brand, 1972). How does the hemolymph return to the gill and the heart? We found the outlet of the foot chamber just underneath the hinge, and the pathway of venous return to the heart is summarized in Fig. 6B. The outlet is connected with the hinge ligament duct. The hinge ligament duct initiates from the teeth of the hinge. The space between the teeth of *Akebiconcha* was documented by Horikoshi (1987), and named the 'subumbonal pit' (Fig. 2H). Horikoshi (1987) also found the structure of the hinge ligament duct, but could not specify the physiological function of the subumbonal pit and the hinge ligament duct. Now, we propose that these are the main route of the venous return to the heart from the foot. The hinge ligament duct is protected by the hinge ligament, a pair of shells and the pericardium. Therefore, this route is safe from the pressure or motion of the visceral organs, and allows the maintenance of a constant venous return to the gills and the heart. The subumbonal pit was found not only in *Vesicomyidae*, but also in *Arcticidae*, *Cyclina* and *Saxidomus* (Horikoshi, 1987; Horikoshi and Hashimoto, 1992). Thus, it will be necessary to conduct future studies on the structure and function of the subumbonal pit and the hinge ligament duct.

Testing the inflatable fastener bag model by circulation during foot extension and retraction

Foot extension and retraction conducted in the inflatable fastener bag model can be summarized as follows. (1) During the resting state, the inflow and outflow of hemolymph in the inflatable fastener bag are balanced, so that the foot maintains a constant volume (Fig. 6A). (2) Foot extension starts from the contraction of muscles in the fastener zone so that flow of the pedal arteries and pedal sinuses is stopped, and the hemolymph volume of the inflatable fastener bag is maintained. The pressure of hemocoel in the inflatable bag is increased by contraction of the pedal circular muscles, and the anterior retractor muscle contracts so that the foot extends (Fig. 6A). (3) Foot retraction starts from the relaxation of muscles in the fastener zone so that hemolymph returns to the visceral reservoir. Outflow via the hinge ligament duct then continues. The volume and pressure of the inflatable bag decreases, and the posterior retractor muscle contracts, so that the foot is retracted (Fig. 6A).

In order to test this model, we need to measure: (1) changes in the volume and flow in the foot and (2) changes in pressure in the vessels and the foot. It would be best if we could detect any increase or decrease in the volume of the inflatable fastener bag. In principle, we should be able to detect changes in the foot volume by employing 3D T_{1w}-MRI, because we would not expect the position and shape of the foot to change, especially to a position outside the shell. However, because of the technical limitations of MRI, we could not detect 3D T_{1w}-MRI every second. For example, 20.48 s are required to obtain 3D data matrix of 64×64×32 with T_R=10 ms. Therefore, we detected movement of the foot from the area of the foot in the 2D T_{1w}-MR images and estimated changes in the flow from the T_{1w}-MR image intensity, as shown in Fig. 5A. During the resting state, the area of the foot and the flow were relatively constant, which indicated that the inflow and outflow of the hemolymph in the foot are balanced. In the beginning of the extension, the image intensity of the fastener zone increased transiently 3 times (‡ and § in Fig. 5Aii). The first and the second peaks occurred with almost the same timing as diastole of the heart, and we also detected several high-intensity spots (‡ in Fig. 5Bb), reflecting an increase in the venous flow in the fastener zone. However, the timing of the third peak was delayed from diastole of

Journal of Experimental Biology (2023) 226, jeb244857. doi:10.1242/jeb.244857

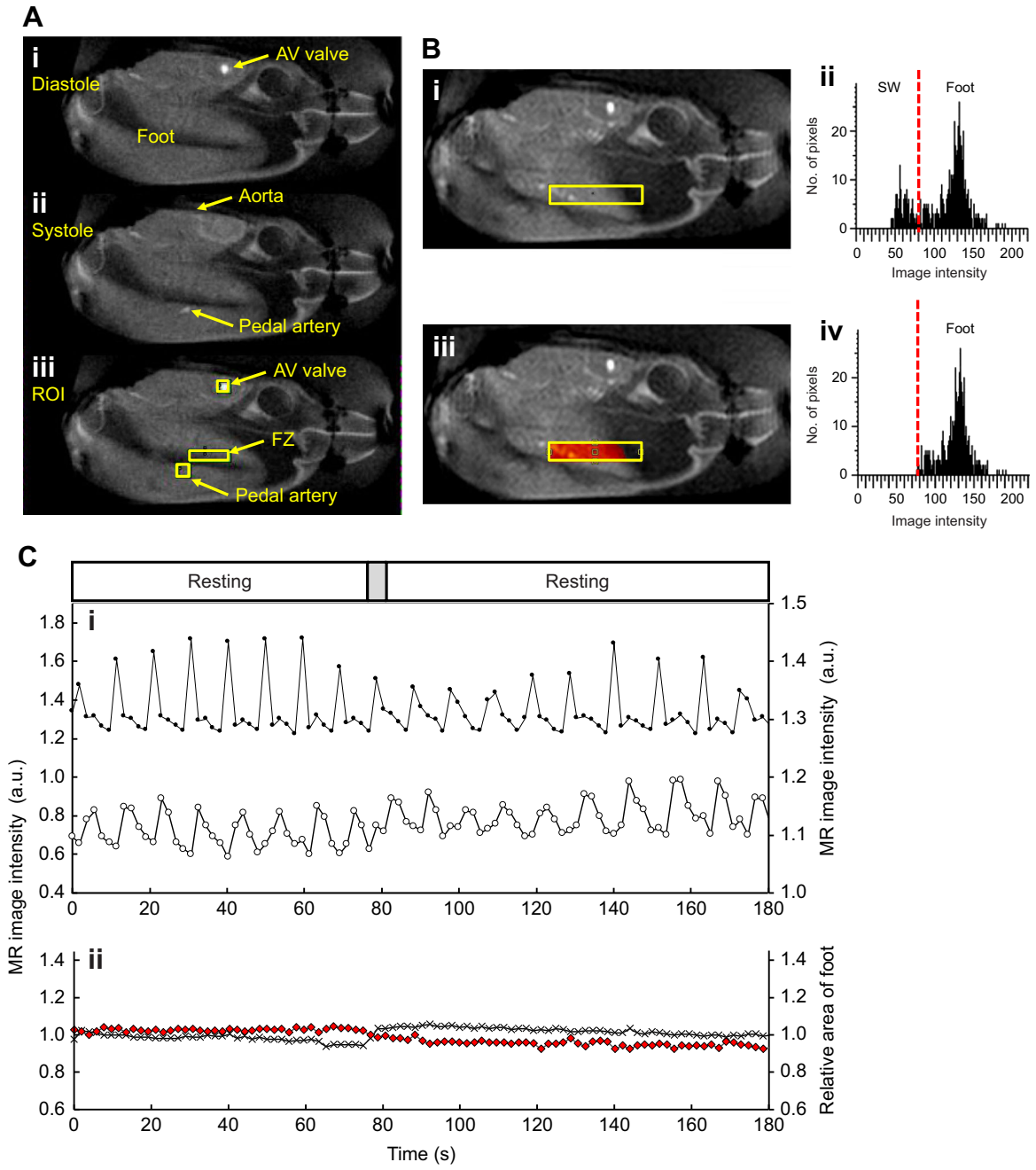

Fig . 4. Heartbeat, hemolymph flow in the pedal artery and foot, and movement of the foot of *C. okutanii* in the resting state. (A) Detection of the heartbeat and flow in a mid-sagittal image of the clam. (i) Diastole of the heart. The high-intensity image of the AV valve indicates the inflow from the auricle to the ventricle. (ii) Systole of the heart. The high-intensity image of the aorta and the pedal artery indicates ejection of the hemolymph from the ventricle. (iii) Regions of interest (ROI) for the measurement of hemolymph flow. Yellow rectangles indicate ROI for the AV valve, pedal artery and a part of the FZ. (B) Detection of extension and retraction of the foot. (i) A ROI positioned in the foot, chosen so that it could cover movement of the foot from the resting state to the full extension of the foot. (ii) Histogram of the number of pixels in the ROI from the high-intensity image shown in i. The foot showed a higher signal intensity compared with the seawater (SW) in the mantle cavity. (iii) ROI in the foot, showing the number of pixels (in red) compared with the threshold (30% of the maximum). (iv) Histogram of the number of pixels in the ROI from the high-intensity image shown in iii. (C) Typical heartbeats in the resting state. The gray area indicates minimal movement of the foot. (i) T_{1w}-MR image intensity of the AV valve (filled circles) and the hinge ligament duct (open circles) plotted every 1.92 s. The heartbeat was regular with a heart rate of 6.0±0.5 beats min^{-1} (18 heartbeats). (ii) Relative area of the foot (red diamonds) and image intensity of the FZ (crosses) plotted every 1.92 s.

the heart, and because it was also shown as a single spot (§ in Fig. 5Bc), this reflected an increase in arterial flow in the fastener zone. Therefore, in the beginning of extension, it is likely that the flow of the pedal sinus increased, but is soon stopped, while inflow from the pedal artery continues. As a result, the volume of inflatable fastener bag increases until the arterial flow is stopped by the fastener zone muscle. During the later part of the extension, the image intensity of the fastener zone gradually decreased, which was probably due to blockage of the flow by the muscle in the fastener zone (Fig. 5Aii). Indeed, the cardiac output almost stopped for 60 s

Journal of Experimental Biology (2023) 226, jeb244857. doi:10.1242/jeb.244857

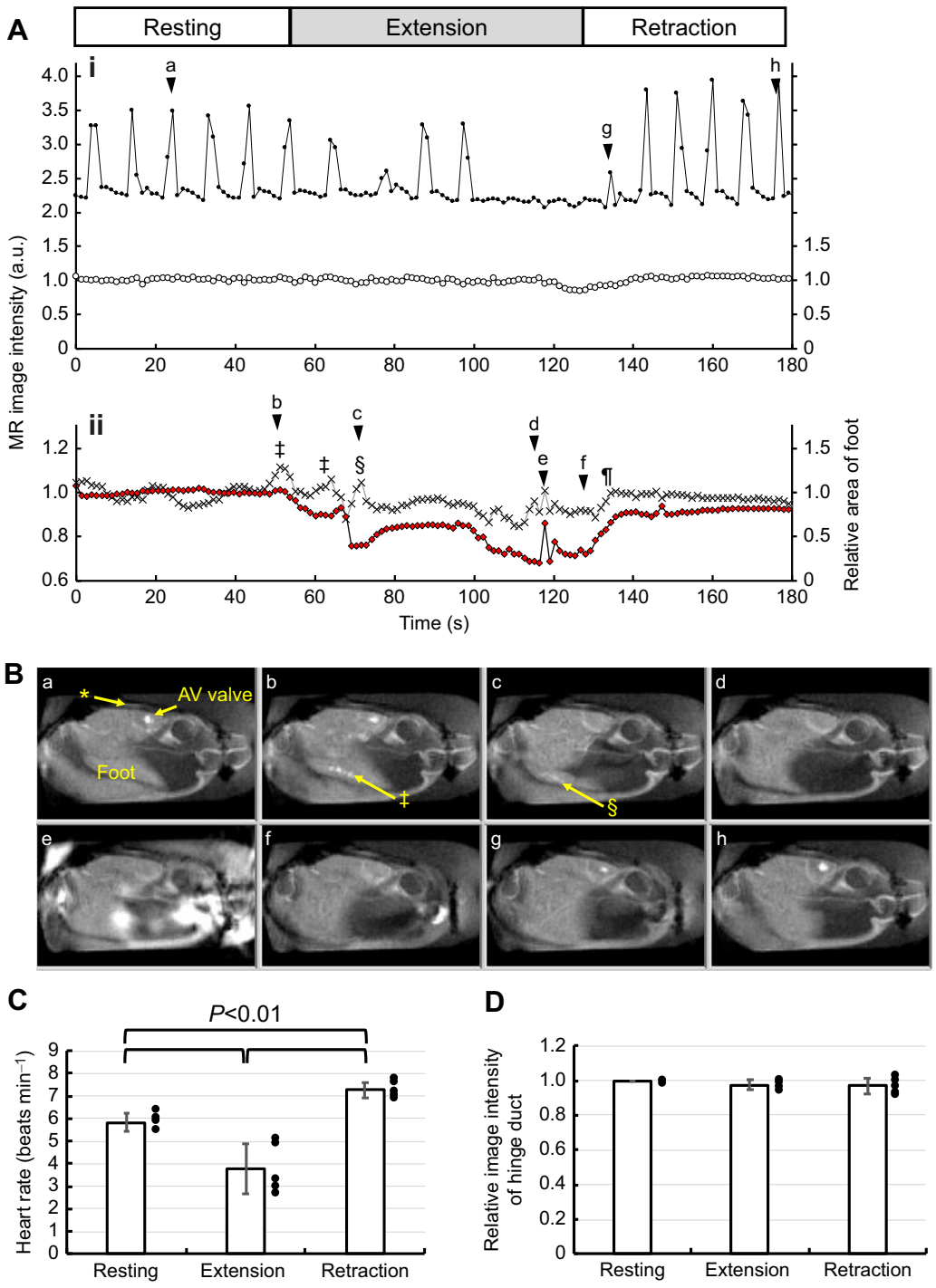

Fig. 5. Foot movement-related changes in heartbeat of *C. okutanii*. (A) Changes in heartbeat due to extension and retraction of the foot. (i) T_{1w}-MR image intensity of the AV valve (filled circles) and the hinge ligament duct (open circles) plotted every 1.28 s. Heart rate in the resting state, and during extension and retraction of the foot was 6.0±0.4 beats min^{-1} (5 heartbeats), 4.8±2.1 beats min^{-1} (5 heartbeats) and 7.1±0.6 beats min^{-1} (5 heartbeats), respectively. (ii) The relative area of the foot (red diamonds) and the image intensity of the FZ (crosses) plotted every 1.28 s. The timing of the T_{1w}-MRI is shown by the arrowheads labeled a–h. Symbols (‡, § and ¶) indicate an increase in the flow in the foot. (B) Mid-sagittal T_{1w}-MR images at rest (a), during foot extension (b–f), and during foot extension and at rest (g,h). The asterisk indicates the hinge ligament duct. Symbols (‡ and §) indicate an increase of flow in the FZ. Refer also to Movie 3. (C) Mean (±s.d.) heart rate of 5 sets of foot movements observed in 3 clams. Individual values are also shown by filled circles beside the bars. Statistical differences were detected for 3 groups, and also for all combinations (P<0.01). (D) Relative T_{1w}-MR image intensity of the hinge ligament duct, compared with the resting state. Individual values are also shown by filled circles beside the bar. No statistical differences were detected, compared with 1.0 (resting state) (P>0.05).

in the last part of extension of the foot (Fig. 5Ai). This was caused by an increase in the output resistance as a result of the increase in the pressure in the inflatable fastener bag. At the start of retraction of the foot, the image intensity of the fastener zone increased with almost the same timing (¶ in Fig. 5Aii), and the cardiac diastole restarted 6 s later (g in Fig. 5Ai). These findings show the increase

Journal of Experimental Biology (2023) 226, jeb244857. doi:10.1242/jeb.244857

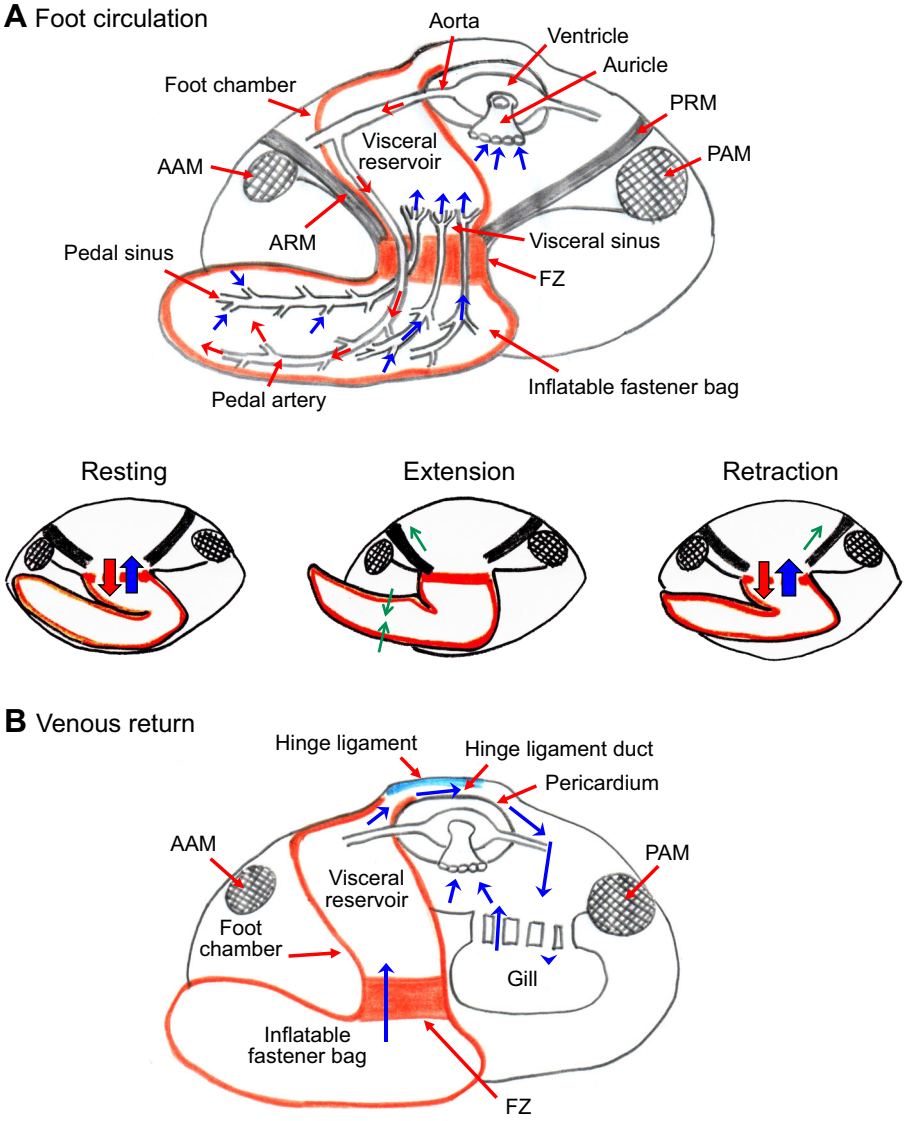

Fig. 6. Schematic diagram of a model of the foot and circulation system of *C. okutanii* in the mid-sagittal section. (A) Top: schematic diagram of foot circulation. The direction of the arterial and venous hemolymph streams is shown by red and blue arrows, respectively. The thick red line indicates the wall of the foot chamber. For clarity, the digestive organs and gills have been omitted. Bottom: schematic diagram of flow in the fastener zone. At rest, inflow and outflow of hemolymph are balanced. During extension, outflow and inflow stop, and the pedal circular muscles and ARM contract (green arrows). During retraction, outflow increases, and the PRM contract (green arrow). (B) Schematic diagram of venous return. The direction of the venous hemolymph streams is shown by blue arrows. The thick blue line indicates the hinge ligament. The hinge ligament duct consists of the hinge ligament, a pair of shells and the pericardium. AAM, anterior adductor muscle; PAM, posterior adductor muscle.

in the venous return from the inflatable fastener bag. We did not detect any significant increase in the flow in the hinge ligament duct during foot extension (Fig. 5D). This was probably because of the large volume of the visceral reservoir, so that the flow in the hinge ligament duct was steady, unlike the pulsed flow of the visceral sinus of *Nodularia* (Seo and Seo, 2019). Judging by these results, changes in the flow and the area of the foot agree well with the inflatable fastener bag model.

The major limitation of this study was that we did not directly measure the pressure in the vessels or the foot. Instead, we indirectly estimated changes in pressure from the heart rate using Frank–Starling's law of the heart. According to that mechanism, cardiac output is determined by the venous return (Guyton and Hall, 2006). Cardiac output is the product of heart rate and stroke volume. Stroke volume is the volume of the hemolymph output for one heartbeat. In cases where the stroke volume, which is considered the contractility of the heart, is constant, cardiac output is proportional to heart rate. Based on the inflatable fastener bag model, during foot extension, it is expected that the venous return from the inflatable fastener bag will decrease. In addition, the resistance of the pedal artery should increase, as a result of the increase in pressure in the inflatable fastener bag. Thus, cardiac output decreases as a consequence of the decrease in the venous return, and also due to the increase in resistance. Therefore, heart rate must decrease during the muscle extension. Vice versa, during foot retraction, the resistance of the pedal artery decreases and the venous return from the inflatable fastener bag increases. Brand (1972) and Sommerville (1975) measured the ventricular pressure of *Anodonta*, and explained the slowing in the heart rate during extension of the foot as pressure build up in the foot due to closure of Keber's valve. Therefore, heart rate must increase during muscle retraction. As shown in Fig. 5C, heart rate did decrease during muscle extension, and increased during retraction, compared with the resting state, a result that agrees well with the hypothesis of the inflatable fastener bag model.

Another limitation of this study is the *C. okutanii* species itself. This clam lives in deep-sea water, and the clam is one of most difficult species to maintain in normal atmospheric conditions, so it is necessary to conduct experiments within a few days of sampling (Miyake et al., 2012; Seo et al., 2022). Therefore, further investigation into this mechanism should be performed with species without any Keber's valve that are easier to obtain and to

maintain in laboratory conditions: that is, clams that live in shallow water.

In conclusion, our study indicates that *C. okutanii* could control foot extension and retraction without Keber's valve. The distal part of the foot forms the inflatable fastener bag, and the volume is controlled by flow of the pedal sinus by the contraction of muscles in the fastener zone. This is an alternative mechanism for the control of foot motion. Hemolymph from the foot is pooled once in the visceral reservoir. Then, the hemolymph passes through the hinge ligament duct to the gill and the heart. The hinge ligament duct can maintain the route of the venous return of the hemolymph. This is a new physiological role of the hinge of bivalves. Thus, it will be necessary to conduct future studies on the hinge structure and function of bivalves.

Acknowledgements
The authors would like to express their sincere thanks to Dr T. Okutani for providing helpful comments. We would also like to express our thanks to Dr Y. Kamei, Ms M. Saida, Ms C. Ichikawa and Ms M. Asao (the Optics and Imaging Facility, Trans-Scale Biology Center, National Institute for Basic Biology, Okazaki, Japan) for their technical support in relation to observation skills and maintenance of the micro-CT and light microscopy. We must also thank the captains and crew members of the research vessels *Natsushima* and *Kaimei*, and the ROV *Hyper-Dolphin* for sample collections (NT14-05, KM16-04).

Competing interests
The authors declare no competing or financial interests.

Author contributions
Conceptualization: E.S., Y.S.; Methodology: E.S., K.O., Y.I., M.Y., T.Y., Y.S.; Validation: E.S., Y.S.; Investigation: E.S., K.O., Y.I., M.Y., T.Y., Y.S.; Resources: E.S., K.O.; Data curation: E.S., Y.S.; Writing - original draft: E.S., Y.S.; Writing - review & editing: E.S., K.O., Y.S.; Funding acquisition: E.S., Y.S.

Funding
This work was supported by National Institute for Basic Biology Collaborative Research Program (22NIBB509 to Y.S. and E.S.), and Japan Society for the Promotion of Science KAKENHI (JP24659102 to Y.S.).

Data availability
All relevant data can be found within the article and its supplementary information.

References
Ansell, A. D. and Trueman, E. R. (1967). Burrowing in *Mercenaria mercenaria* (L.) (Bivalvia, Veneridae). *J. Exp. Biol.* **46**, 105-115. doi:10.1242/jeb.46.1.105
Bayne, B. L. (1976). *Marine Mussels: Their Ecology and Physiology*. Cambridge: Cambridge University Press.
Bock, C., Frederich, M., Wittig, R.-M. and Pörtner, H.-O. (2001). Simultaneous observations of haemolymph flow and ventilation in marine spider crabs at different temperatures: a flow weighted MRI study. *Magn. Reson. Imaging.* **19**, 1113-1124. doi:10.1016/S0730-725X(01)00414-3
Borradaile, L. A. and Potts, F. A. (1935). *The Invertebrata. A Manual for the Use of Students*, 2nd edn. Cambridge: Cambridge University Press.
Brand, A. R. (1972). The mechanism of blood circulation in *Anodonta anatina* (L.) (Bivalvia, Unionidae). *J. Exp. Biol.* **56**, 361-379. doi:10.1242/jeb.56.2.361
Childress, J. J., Fisher, C. R., Favuzzi, J. A., Arp, A. J. and Oros, D. R. (1993). The role of a zinc-based, serum-borne sulphide-binding component in the uptake and transport of dissolved sulphide by the chemoautotrophic symbiont-containing clam *Calyptogena elongata*. *J. Exp. Biol.* **179**, 131-158. doi:10.1242/jeb.179.1.131
Guyton, A. C. and Hall, J. E. (2006). *Textbook of Medical Physiology*, 11th edn, p. 1116. Philadelphia: Elsevier Saunders.
Hashimoto, J. and Okutani, T. (1994). Four new *Mytilid* mussels associated with deepsea chemosynthetic communities around Japan. *Venus* **53**, 61-83.
Horikoshi, M. (1987). Distinctions in the hinge structure between *Akebiconcha* and *Calyptogena*, with special reference to "Subumbonal Pit" and "Cardinal Ligament". *Venus* **45**, 245-257. doi:10.18941/venusjjm.45.4_245
Horikoshi, M. and Hashimoto, J. (1992). Two distinct growth stages of deep-sea, giant white clam, "*Calyptogena*" *soyoae*, and its allied species. *La mar* **30**, 73-82.
Kanda, Y. (2013). Investigation of the freely available easy-to-use software 'EZR' for medical statistics. *Bone Marrow. Transplant.* **48**, 452-458. doi:10.1038/bmt.2012.244
Keber, G. A. F. (1851). *Beiträge zur Anatomie und Physiologie der Weichthiere*. Königsberg: C. R. Wilhelmi.
Klylova, E. M. and Sahling, H. (2006). Recent bivalve molluscs of the genus *Calyptogena* (Vesicomyidae). *J. Moll. Stud.* **72**, 359-395. doi:10.1093/mollus/eyl022
Kojima, S. (2002). Deep-sea chemoautosynthesis-based communities in the northwestern Pacific. *J. Oceanogr.* **58**, 343-363. doi:10.1023/A:1015869927288
Kojima, S. and Ohta, S. (1997). *Calyptogena okutanii* n. sp., a sibling species of *Calyptogena soyoae* Okutani, 1957 (bivalvia: Vesicomydae). *Venus* **56**, 189-195.
McMahon, B. R., Wilkens, J. L. and Smith, P. J. (2011). Invertebrate circulatory systems. In *Handbook of Physiology, Section 13, Comparative Physiology* (ed. W. H. Dantzler), pp. 931-1008. American Physiological Society. doi:10.1002/cphy.cp130213
Miyake, H., Kitada, M., Lindsay, D. J., Itoh, T., Nemoto, S. and Miwa, T. (2012). How to keep deep-sea animals. In *Diversity of Ecosystems* ed.(M. Ali), pp. 51-72. London: IntechOpen. http://www.intechopen.com/books/diversity-of-ecosystems/how-to-keep-deep-sea-animals.
Morton, J. E. (1964). Locomotion. In *Physiology of Mollusca, Volume I* (ed. K. M. Wilbur and C. M. Yonge), pp. 383-423. New York: Academic Press.
Prudie, A. (1887). *The Anatomy of the Common Mussels (mytilus latus, edulis, and magellanicus)*. New Zealand: Colonial Museum and Geological Survey Department. (Republished in 2012 by Ulan Press).
Ruppert, E. E., Fox, R. S. and Barnes, R. D. (2015). *Invertebrate Zoology: A Functional Evolutionary Approach*. New Delhi: Cengage.
Schwanecke, H. (1913). Das Blutgefäßsystem von Anodonta cellensis Schröt. *Z. Wiss. Zool.* **107**, 1-77.
Seo, E. and Seo, Y. (2019). Roles of Keber's valve and foot chamber for foot manipulation in the mussel *Nodularia douglasiae*. *Biol. Open* **8**, bio039859. doi:10.1242/bio.039859
Seo, E., Ohishi, K., Maruyama, T., Imaizumi-Ohashi, Y., Murakami, M. and Seo, Y. (2014a). Testing the constant-volume hypothesis by magnetic resonance imaging of the mussel heart in the *Mytilus galloprovincialis*. *J. Exp. Biol.* **217**, 964-973. doi:10.1242/jeb.092577
Seo, E., Ohishi, K., Maruyama, T., Imaizumi-Ohashi, Y., Murakami, M. and Seo, Y. (2014b). Magnetic resonance imaging analysis of water flow in the mantle cavity of live *Mytilus galloprovincialis*. *J. Exp. Biol.* **217**, 2277-2287. doi:10.1242/jeb.101949
Seo, E., Maruyama, T. and Seo, Y. (2022). Cardiac function of the deep-sea bivalve, Calyptogena okutanii, observed at atmospheric pressure via magnetic resonance imaging. *Deep-Sea Res I.* **186**, 103826. doi:10.1016/j.dsr.2022.103826
Sommerville, B. A. (1975). Factors affecting the heart activity and blood pressure of the swan mussel *Anodonta cygna*. *J. Exp. Biol.* **62**, 341-355. doi:10.1242/jeb.62.2.341
Trueman, E. R. (1966). The fluid dynamics of the bivalve molluscs, *Mya* and *Margaritifera*. *J. Exp. Biol.* **45**, 369-382. doi:10.1242/jeb.45.2.369
Trueman, E. R. (1983). Locomotion in Molluscs. In *The Mollusca, Volume 4: Part 1* (ed. A. S. M. Saleuddin and K. L. Wilbur), pp. 155-198. London: Academic Press.
Trueman, E. R. and Brown, A. C. (1985). Dynamics of burrowing and pedal extension in *Donax serra* (Mollusca: Bivalvia). *J. Zoology* **207**, 345-355. doi:10.1111/j.1469-7998.1985.tb04936.x
Trueman, E. R., Brand, A. A. and Davis, P. (1966). The dynamics of burrowing of some common littoral bivalves. *J. Exp. Biol.* **44**, 469-492. doi:10.1242/jeb.44.3.469
Trueman, E. R., Brown, A. C. and Stenton-Dozey, J. (1986). Blood flow in a burrowing bivalve at pedal extension and retraction. *J. Moll. Stud.* **52**, 265-266. doi:10.1093/mollus/52.3.265
Watanabe, H., Seo, E., Takahashi, Y., Yoshida, T., Kojima, S., Fujikura, K. and Miyake, H. (2013). Spatial distribution of sister species of vesicomyid bivalves *Calyptogena okutanii* and *Calyptogena soyoae* along an environmental gradient in chemosynthetic biological communities in Japan. *J. Oceanogr.* **69**, 129-134.
Willem, V. and Minne, A. (1898). Recherches expérimentales sur la circulation sanguine chez l'Anodonte. *Mém. cour. Mém. Sav. étr.* **57**, 3-28.
Winter, A. G., 5th, Deits, R. L. and Hosoi, A. E. (2012). Localized fluidization burrowing mechanics of *Ensis directus*. *J. Exp. Biol.* **215**, 2072-2080. doi:10.1242/jeb.058172

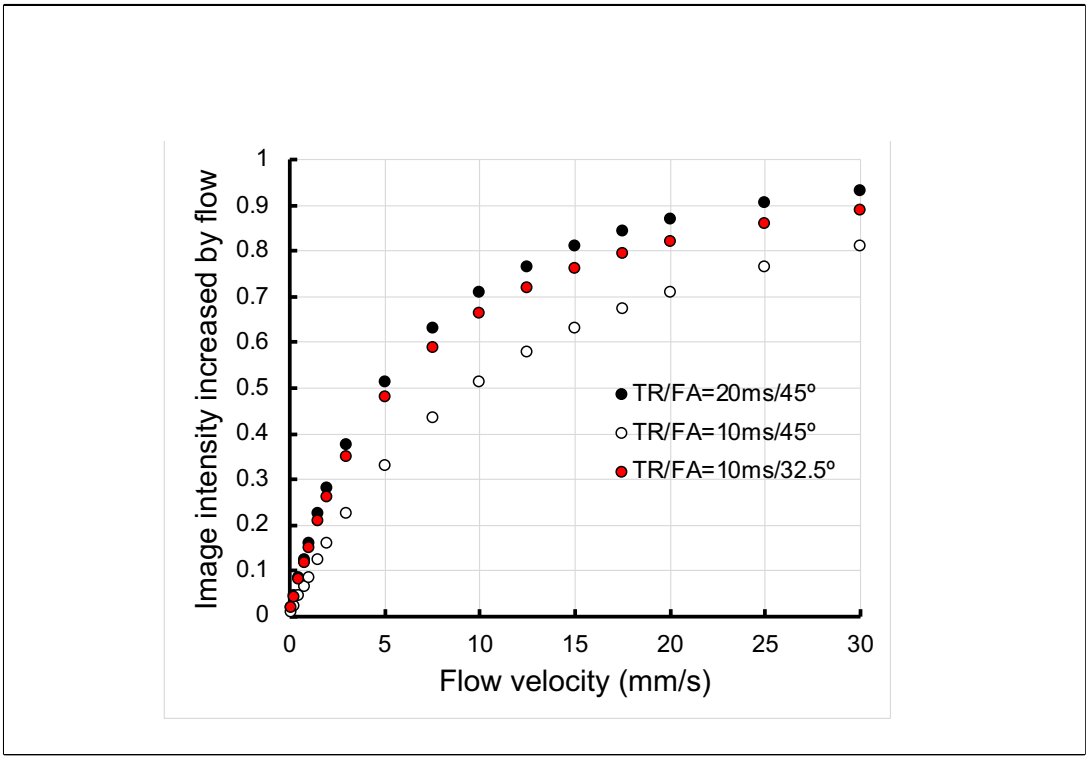

Fig. S1. lip angle dependency of the relationship between flow velocity and image intensity.

Increase of T_{1W}-MR image intensity due to flow were calculated by the function:

$$M(V)/(Mo \cdot \sin\theta)$$

$$= [1 - \exp(-TR \cdot k \cdot V)] / [\, 1 - \cos\theta \cdot \exp(-TR \cdot k \cdot V)]$$

where θ, TR, V, k are flip angle (FA), relaxation delay, flow velocity and a constant, respectively. Mo is the equilibrium magnitude. The k value (27) was obtained by the flow experiment of the seawater (Seo et al., 2014b).

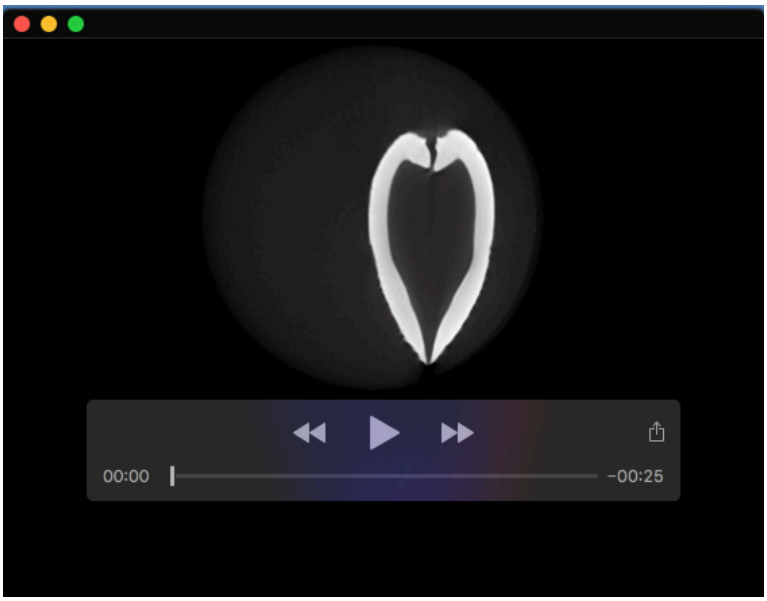

Movie 1. Transverse micro CT of *Calyptogena okutanii* around the hinge area. A series of 405 images from the anterior to posterior of the clam were shown every 47 μm.

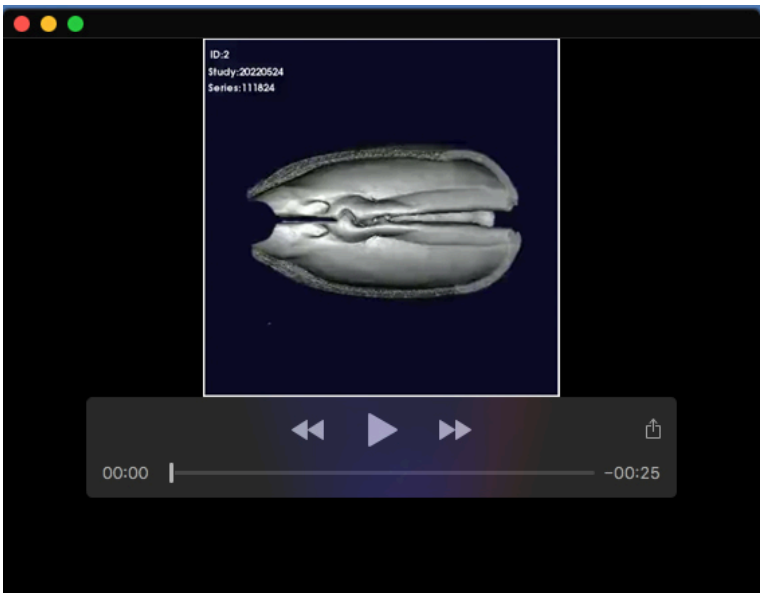

Movie 2. 3D reconstructed micro CT and T_{1w}-MRI of *Calyptogena okutanii.*
(A) 3D reconstructed micro CT around the hinge area of the clam shown in Fig. 2A. A series of 36 images were rotated in 10 degree steps around the left-right axis.
(B) 3D reconstructed T_{1w}-MRI of hemolymph and visceral tissues around the hinge area of the clam shown in Fig. 2C. A series of 24 images were rotated in 15 degree steps around the dorsal-ventral oblique axis.

Journal of Experimental Biology • Supplementary information

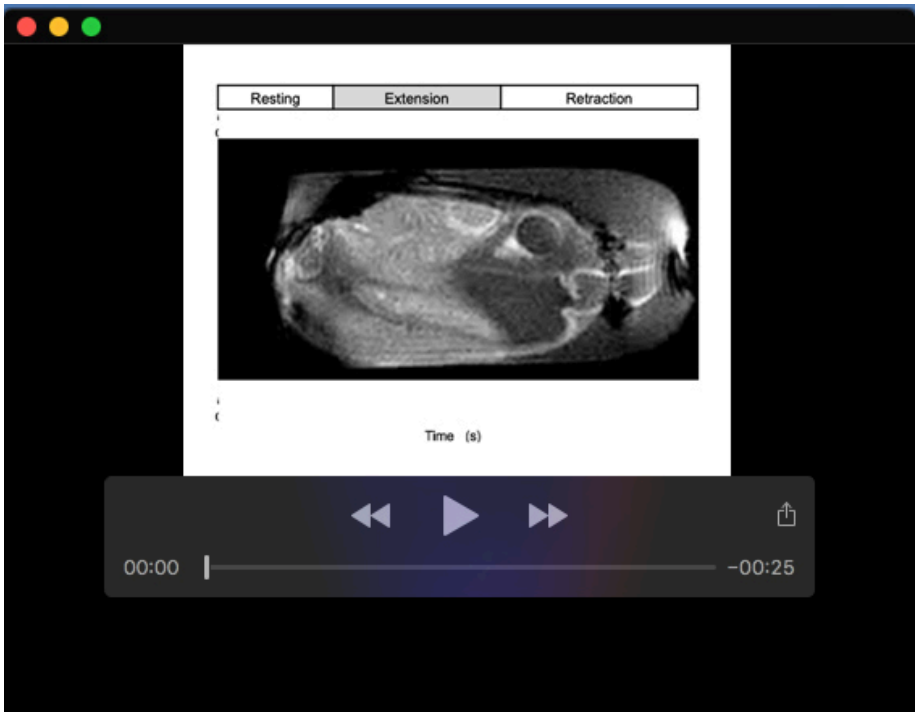

Movie 3. Mid-longitudinal T_{1w}-MRI of heartbeat of *Calyptogena okutanii* measured every 1.2 s shown in Fig. 5A. A series of 173 images were obtained at 5 frames s^{-1}.